Journal of
Synchrotron Radiation

ISSN 0909-0495

Received 29 May 2008
Accepted 2 December 2008

Mini-beam collimator enables microcrystallography experiments on standard beamlines

Robert F. Fischetti,[a]* Shenglan Xu,[a] Derek W. Yoder,[a] Michael Becker,[a] Venugopalan Nagarajan,[a] Ruslan Sanishvili,[a] Mark C. Hilgart,[a] Sergey Stepanov,[a] Oleg Makarov[a] and Janet L. Smith[a,b]

[a]GM/CA CAT at the APS, Biosciences Division, Argonne National Laboratory, Argonne, IL 60439, USA, and [b]Life Sciences Institute, Department of Biological Chemistry, University of Michigan, Ann Arbor, MI 48109, USA. E-mail: rfischetti@anl.gov

The high-brilliance X-ray beams from undulator sources at third-generation synchrotron facilities are excellent tools for solving crystal structures of important and challenging biological macromolecules and complexes. However, many of the most important structural targets yield crystals that are too small or too inhomogeneous for a 'standard' beam from an undulator source, ~25–50 μm (FWHM) in the vertical and 50–100 μm in the horizontal direction. Although many synchrotron facilities have microfocus beamlines for other applications, this capability for macromolecular crystallography was pioneered at ID-13 of the ESRF. The National Institute of General Medical Sciences and National Cancer Institute Collaborative Access Team (GM/CA-CAT) dual canted undulator beamlines at the APS deliver high-intensity focused beams with a minimum focal size of 20 μm × 65 μm at the sample position. To meet growing user demand for beams to study samples of 10 μm or less, a 'mini-beam' apparatus was developed that conditions the focused beam to either 5 μm or 10 μm (FWHM) diameter with high intensity. The mini-beam has a symmetric Gaussian shape in both the horizontal and vertical directions, and reduces the vertical divergence of the focused beam by 25%. Significant reduction in background was achieved by implementation of both forward- and back-scatter guards. A unique triple-collimator apparatus, which has been in routine use on both undulator beamlines since February 2008, allows users to rapidly interchange the focused beam and conditioned mini-beams of two sizes with a single mouse click. The device and the beam are stable over many hours of routine operation. The rapid-exchange capability has greatly facilitated sample screening and resulted in several structures that could not have been obtained with the larger focused beam.

Keywords: mini-beam; microbeam; microdiffraction; macromolecular crystallography.

1. Introduction

Given the vagaries of crystal growth of biological macromolecules, the need to determine structures from the smallest obtainable crystals is clear. Additionally, many samples are inhomogeneous but have small, well ordered, homogeneous zones that would produce useful diffraction if selectively irradiated. Although a reduced beam size will by definition yield weaker diffraction than a standard beam because it irradiates fewer unit cells, the usefulness of a mini-beam in macromolecular crystallography is by now well documented, particularly by the pioneering work at ID-13 at the ESRF (Pebay-Peyroula *et al.*, 1997; Weichendrieder *et al.*, 2000; Fotinou *et al.*, 2001; Renault *et al.*, 2001; Zhou *et al.*, 2001; Xiao *et al.*, 2003). We define a mini-beam as having dimensions of 5–10 μm. The first dedicated mini-beam station for protein crystallography incorporated a microdiffractometer upstream of the normal diffractometer at beamline X06SA of the Swiss Light Source (SLS) (http://sls.web.psi.ch/view.php/beamlines/px/endstations/index.html). The crystal structure reported from the smallest crystals to date was solved using data from this station (Coulibaly *et al.*, 2007).

Existing micro/mini-beam efforts around the world are of two types: those that directly focus some or all of the incident beam to a small beam, and those that overfill a small aperture near the sample, thereby providing a small beam that is relatively stable but with no increase in flux density relative to the standard beam. A variety of focusing optics have been used to produce micrometer-sized beams at ID-13 at the ESRF (Riekel, 2004; Riekel *et al.*, 2005; Nelson *et al.*, 2005;

Moukhametzianov *et al.*, 2008). A focused 20 µm mini-beam has been implemented at MacCHESS using capillary focusing optics, which are most appropriate for a second-generation light source (Huang & Bilderback, 2006). A focused 7 µm mini-beam is in routine use at ESRF beamline ID23-2 (http://www.esrf.eu/UsersAndScience/Experiments/MX/About_our_beamlines/ID23-2/Technical_Overview). A pair of short Kirkpatrick–Baez mirrors placed close to the sample defines this mini-beam, at the cost of increased beam divergence owing to the high demagnification ratio. Most aperture-defined devices are based on a micrometer-sized shaping system that was developed several years ago at ESRF ID13 to produce clean beams down to 10 µm size from the 20 µm × 40 µm focused beam size (Perrakis *et al.*, 1999; Cipriani *et al.*, 2007). This diffractometer, which features an air-bearing goniometer and microscope co-axial with the X-ray beam, is now available commercially (http://www.accel.de/News/microdiffractometer.html). The commercial diffractometer is in use at SLS beamline X06SA to condition the focused beam (5 µm × 25 µm). This beamline also has an infrequently used capability to produce a mini-beam by focusing.

Although small beams are of great interest to the user community, no mini-beam (5–10 µm) was available in the USA when this project was initiated. To fill this void, we developed a mini-beam capability on the two tunable GM/CA-CAT insertion device (ID) beamlines 23-ID-B and 23-ID-D of the APS. A single-collimator prototype was developed in early 2007 and made available to all users in Fall 2007. The triple-beam device was implemented for all users in February 2008. Other mini-beam developments are now underway in the USA; most employ the commercial diffractometer.

Here we describe a simple device to define a mini-beam of 5 µm or 10 µm diameter and the characterization of these mini-beams. Individual mini-beam apparatuses can be exchanged and aligned in about 15 min. A new triple mini-beam apparatus under software control allows users to switch rapidly among the standard beam and the two mini-beams. Applications of the mini-beam have been described elsewhere (Sanishvili *et al.*, 2008), and a predecessor of the new device was described in 2007 (Xu & Fischetti, 2007).

2. Methods

2.1. Mini-beam collimator

An exploded view of the mini-beam apparatus is shown in Fig. 1(*a*). The X-ray beam propagates from right to left. The beam size is defined by a 2 mm-diameter platinum disk with a pinhole in the center (Ted Pella, Inc.). The disk is 600 µm thick and tapers to 150 µm at the position of the aperture. The pinhole is located directly above the 39 mm mark on the ruler in the figure and is shown lying on its side for clarity. A beam size as small as 5 µm can be defined at the sample position by inserting a pinhole with appropriate aperture into the bullet-shaped molybdenum scatter guard [3.20 mm outer diameter (OD), 2.05 mm inner diameter (ID)], which captures scatter in all but the forward and backward directions. We typically use

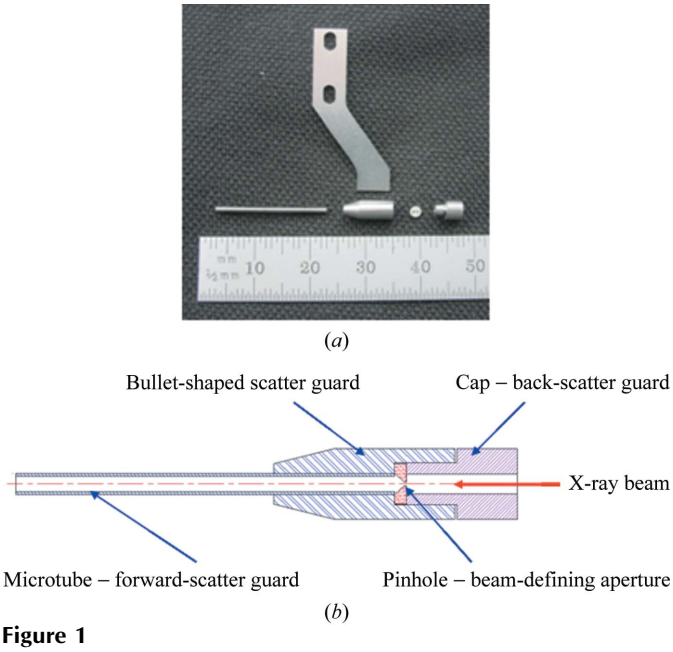

Figure 1
Components of the mini-beam collimator. (*a*) Exploded view of the mini-beam collimator and support. The direction of beam travel through the components is from right to left. The collimator components are the Mo back-scatter guard (positioned at the 46 mm mark on the ruler), the beam-defining Pt pinhole (39 mm), the bullet-shaped scatter guard (30 mm) and the forward-scatter guard tube (12 mm). The pinhole is on its side in this picture for clarity. The stainless steel arm (above the collimator components) connects the assembled collimator to the kinematic carrier (Fig. 2). (*b*) Schematic diagram of the assembled mini-beam collimator. Excellent scatter protection is achieved by nesting of the pinhole, back-scatter guard and forward-scatter tube inside the bullet-shaped scatter guard.

5 µm and 10 µm pinholes to define the beam size and a 300 µm pinhole to serve as a scatter guard for the focused 'standard' beam, which is defined by focusing mirrors and/or upstream slits. To minimize the escape of back-scatter, a Mo back-scatter guard (located at 45 mm on the ruler) with a 5.4 mm-deep 1.0 mm-diameter entrance aperture is inserted into the bullet-shaped scatter guard to the right of the Pt pinhole. A long thin tube defines the exit aperture for forward scatter from the pinhole and minimizes air scatter between the pinhole and the sample. The tubes are made of tungsten or Mo (Goodfellow, Inc.) of varying OD/ID to best match the size of the pinhole: the OD of 1.00 mm and ID of 400 µm for the 5 µm and 10 µm pinholes; the OD of 1.05 mm and ID of 790 µm for the 300 µm pinhole. When the device is fully assembled, the back-scatter guard, pinhole, forward-scatter tube and bullet-shaped scatter guard form a compact well shielded mini-beam collimator (Fig. 1*b*).

To address the needs of users who frequently switch between the standard beam and a mini-beam, we also designed and constructed a triple collimator, including 5 µm, 10 µm and 300 µm apertures (Fig. 2). In the triple collimator the Mo scatter guard is a three-way block into which the apertures, forward-scatter tubes and back-scatter guards are inserted. The Mo-block scatter guard has the same function as the bullet-shaped scatter guard in the single mini-beam collimator.

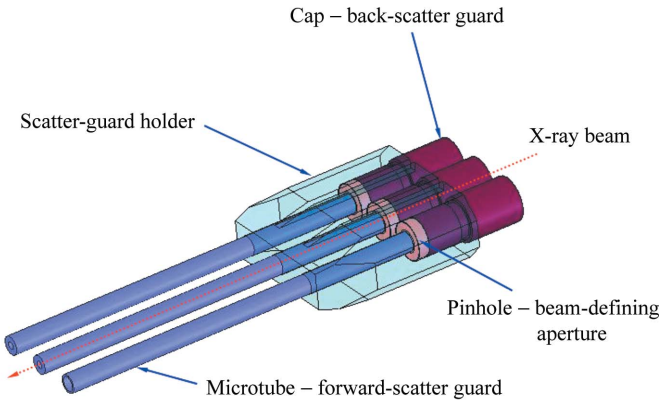

Figure 2
Schematic diagram of the triple collimator. Each collimator consists of a beam-defining pinhole, a forward-scatter tube and a back-scatter guard. These are mounted in a three-way Mo scatter guard.

The tolerance specification for the diameter of the pinholes is ± 1 µm. The true diameters were measured with a CNC Video Measuring System (VMR-3020, Nikon). The measured sizes of the pinholes used in the triple collimator on 23-ID-B are 4.8 µm for the 5 µm pinhole and 9.7 µm for the 10 µm pinhole.

2.2. Kinematic mount

The mini-beam collimator is supported by a thin stainless-steel arm braised in a groove on the bullet-shaped scatter guard (Fig. 1*a*). The stainless-steel arm is attached to one-half of an anodized-aluminium kinematic mount referred to as the carrier (Fig. 3). The kinematic carrier is held onto a kinematic base by rare-earth magnets (Fig. 3*a*). The halves of the kinematic mount have three mated connections: (i) a sapphire ball in the base fitting into a conical hole in the carrier; (ii) an adjustable screw in the carrier fitting into a conical groove in the base; and (iii) a second adjustable screw in the carrier fitting onto a plane in the base. The three pairs of rare-earth magnets securely adhere the carrier to the base with a $\sim$1.0 mm gap between the anodized Al pieces. Fig. 3(*b*) shows the fully assembled mini-beam apparatus on an alignment jig. The alignment jig, equipped with a kinematic base, is used to adjust the mini-beam collimator to a well defined position relative to the kinematic mount, and also to pre-align the X-ray optical axis of the mini-beam collimator to be perpendicular to the plane of the kinematic mount. Several mini-beam apparatuses with different pinhole apertures can be assembled and pre-aligned for rapid interchange on the beamlines. A similar jig aligns the triple mini-beam apparatuses.

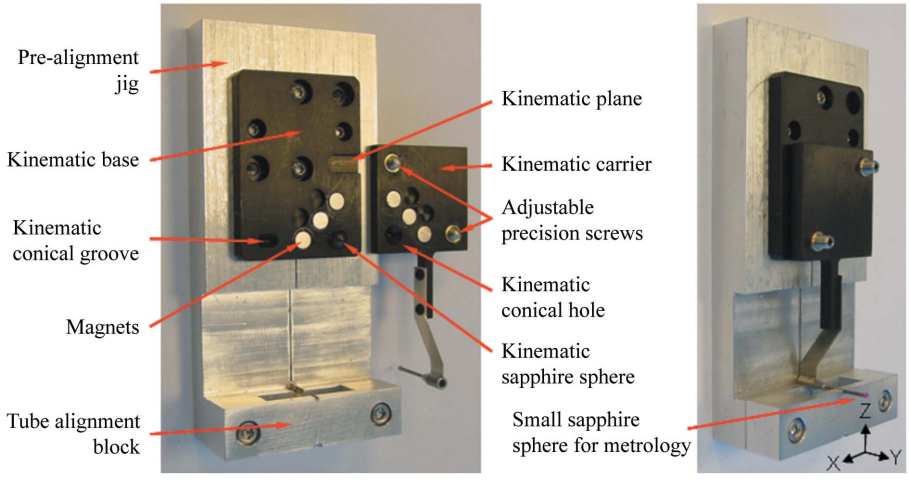

Figure 3
Kinematic mounting of the mini-beam collimator. (*a*) Assembled mini-beam collimator on an exchangeable kinematic carrier, with the halves of the black-anodized Al kinematic mount separated showing details of the mount. The kinematic base is attached to an alignment jig. (*b*) Mini-beam apparatus mounted on the alignment jig. The two halves of the kinematic mount are mated. The bullet-shaped scatter guard and forward-scatter guard tube of the collimator are positioning in the alignment groves. The small sapphire ball at the end of the forward-scatter guard tube was attached only during metrology measurements. The pinhole and back-scatter guard are not shown.

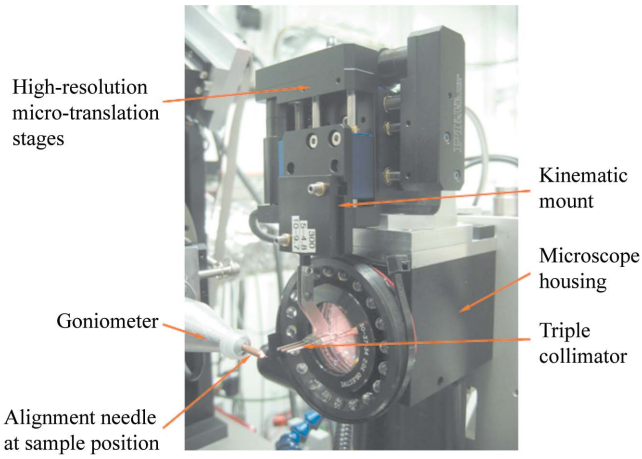

Figure 4
Mini-beam apparatus mounted in the experimental station of beamline 23ID-B. The photograph shows the relationship of the mini-beam positioning motors to the housing for the high-resolution on-axis sample-viewing microscope. An alignment needle is mounted on the sample goniometer at the sample position. The photograph also shows the relationship between the mini-beam collimator and the microscope lens, which are separated by $\sim$0.5 mm.

The triple and single mini-beam apparatuses are positioned on the beamline by another kinematic base (Fig. 4). Alignment of the device and the X-ray beam is achieved by two high-precision motorized stages (Physik Instrumente, Germany, model M-111.1DG), which have a positional reproducibility of 0.1 µm and are encoded to 7 nm resolution. In addition to centering the pinhole on the beam with the stages, the long axis of the forward-scatter tube must be aligned to be coincident with the X-ray beam. This is achieved by adjusting the screws on the kinematic carrier. Thus, individual

carriers can be aligned, removed and reinstalled with submicrometer accuracy (Xu & Fischetti, 2007). The motorized stages are mounted above a high-magnification (×32, 0.30 numeric aperture) on-axis microscope that is used to visualize the sample. The incident X-ray beam goes through the optical axis of the microscope, providing a view of the sample that is free of parallax error. A 1.2 mm hole is bored through the optical axis of the objective lens and through a 45° mirror that deflects the optical axis of the rest of the microscope to be perpendicular to the X-ray axis.

2.3. Scatter guards

To minimize background that reaches the detector owing to air scatter and secondary scatter from the pinhole, the distance between the back-scatter guard of the mini-beam apparatus and the objective lens of the on-axis microscope was reduced to ∼0.5 mm. The end of the forward-scatter tube is 9 mm upstream of the sample position (Fig. 4). This distance was chosen as a compromise that minimizes air scatter between the end of the tube and the sample and simultaneously avoids the cold nitrogen gas stream used to cool the sample.

2.4. Alignment on the beamline

The full X-ray beam is focused by a pair of 'bimorph' mirrors (Signorato *et al.*, 1998; Fischetti *et al.*, 2007) arranged in a Kirkpatrick–Baez geometry. The beam can be focused at the sample position or downstream of the sample to provide a more parallel beam for recording diffraction from crystals with large unit cells. The pitch angle of each mirror is adjustable by motorized stages and a piezo actuator, providing fine control of the beam position in both the horizontal and vertical directions at the sample location.

The focused X-ray beam is aligned to intersect the horizontal rotation axis of the goniometer using a straightforward six-step procedure. (i) The mini-beam collimator is translated vertically to a position above the beam axis, and a fine needle is mounted at the sample position and centered on the rotation axis. (ii) The rotation axis is translated vertically to center the needle on the cross-hairs of the on-axis microscope. (iii) The needle is replaced with a small YAG crystal (Xu *et al.*, 2007) that scintillates when struck by X-rays, allowing one to visualize the beam with the microscope. (iv) The angle of each mirror is adjusted by the piezo actuator to steer the beam to the center of the cross-hairs of the microscope. (v) The mini-beam apparatus is positioned in the beam, reducing the image of the beam on the YAG crystal from a large ellipse to a small circle. (vi) The position of the mini-beam collimator is translated to center the mini-beam on the cross-hairs, and the coordinates are stored. The alignment process has been automated and can be performed in ∼2 min. The mini-beam collimator can be moved out of the beam to a safe position for manual sample mounting, and replaced in the beam path by recalling the stored coordinates. In the event that the beam moves relative to the mini-beam collimator, an automated script can realign the beam by scanning the mirror angles and maximizing the intensity through the mini-beam collimator. After the initial alignment (§2.2) the alignment screws on the kinematic mount rarely need re-adjustment, even after repeated dismount/mount operations. The horizontal or vertical translation of the collimator may need to be adjusted by a few micrometers after manual mounting; however, the triple collimator eliminates the need for manual mounts and dismounts.

3. Results

3.1. Rationale for pinhole approach to mini-beam development

The GM/CA-CAT dual canted undulator beamlines, 23-ID-B and 23-ID-D, are rapidly tunable over a broad energy range. Monochromatic beams on both lines are focused by 'bimorph' mirrors in a Kirkpatrick–Baez geometry, resulting in high demagnification ratios, 6.0:1 horizontal and 7.0:1 vertical for 23-ID-B and 10.0:1 horizontal and 11.8:1 vertical for 23-ID-D (Fischetti *et al.*, 2007). The current minimum size of the focused beam at the sample position is 25 μm vertically and 120 μm horizontally (FWHM) on 23-ID-B, and 20 μm vertically and 65 μm horizontally on 23-ID-D. We evaluated the potential for providing a 5–10 μm mini-beam along several fronts, and based our development of the pinhole apparatus on several factors. Initial tests demonstrated that decreasing the size of the upstream slits did not result in a small enough beam at the sample position (Fig. 5). These slits are ∼230 mm upstream of the sample, and beam divergence from this point resulted in a minimum beam size at the sample position of 16 μm (V) × 38 μm (H) when the slits were closed to their minimum size of 13 μm × 13 μm (Sanishvili *et al.*, 2008). The resulting beam size at the sample position was larger than our 5–10 μm target so other approaches were considered. Very strong focusing optics (∼100:1 demagnification) could be implemented to achieve a mini-focus beam, but the beam divergence from the focal point would increase by an order of magnitude, limiting the largest unit-cell dimension for which diffraction maxima could be resolved. This approach was rejected because of the increase in divergence and concerns about the positional stability of the mini-focus beam. One straightforward path was to configure our goniometer as a mini-beam diffractometer (Perrakis *et al.*, 1999) by installing a small aperture 30 mm upstream of the sample position. Overfilling this aperture would provide beam stability. The intensity through a 10 μm pinhole with the beam focused at the sample position on 23-ID-D was calculated using *XOP* (V2.1, http://www.esrf.eu/computing/scientific/xop2.1/) and *Shadow* (V2.3, http://www.nanotech.wisc.edu/CNT_LABS/shadow.html). These calculations indicated that if the beam is focused to 25 μm × 120 μm at the sample position, then $\sim 3 \times 10^{11}$ photons s^{-1} could be delivered through the 10 μm pinhole, *i.e.* an average flux density of about 10^{16} photons s^{-1} mm^{-2}. Such a beam would provide ample flux for data collection from crystals of macromolecules.

3.2. Kinematic mount

Mini-collimators are mounted on the beamline by means of a kinematic mount (Fig. 3). The robust kinematic mount is a critical part of the mini-beam apparatus because it allows for installation of the device on the alignment jig as well as rapid and highly reproducible transfer of the device to the beamline. The positional reproducibility of the mini-beam collimator on the kinematic mount was determined using optical metrology to record the X and Y positions of a small sapphire sphere glued to the exit of the forward-scatter tube (Fig. 3) (Xu & Fischetti, 2007). The coordinate system is defined in the figure. The RMS deviation from the mean position was 0.24 µm in both the X- and Z-directions for 34 repeated manual mount and dismount operations. The stability of the assembled mount was monitored in the X-direction once per minute over a period of 20 min, and the RMS deviation from the mean X-position was 0.06 µm. The stability in the Z-direction was not measured, but is expected to be smaller than that in the X-direction given the geometry of the support.

3.3. Beam properties

The beam profile was measured at the sample position by scanning a tungsten knife-edge through the beam and recording the transmitted intensity with a PIN diode. The knife-edge was supported on the single-axis horizontal air-bearing goniometer, which carries a pair of high-precision motorized stages (identical to those used to position the mini-beam apparatus) that normally are used for centering sample crystals. The knife-edge scans were performed by scanning the horizontal and vertical support stages of the goniometer assembly. A Gauss error function was fit to the intensity data, providing the best-fit Gaussian profile of the beam (Fig. 6, Table 1). Excellent fits were obtained with a reproducibility of 0.3–0.4 µm in FWHM values over nine scans. The mini-beam size changed only slightly over a wide range of upstream slit settings (Fig. 5). Similarly, as the upstream slits were closed to 50 µm × 50 µm for the 5 µm pinhole and 50 µm × 150 µm for the 10 µm pinhole, the mini-beam intensity recorded at the sample position remained essentially unchanged (>99% of the values when the slits were fully open). Taken together, these data suggest that the pinhole (*i.e.* not the upstream slits) defines the angular convergence of the mini-beam.

The beam intensity at the sample position was determined by converting the current from an ion chamber (10 mm gap, 60 mm path length, N_2 gas, 2500 V) operated in its plateau region. Each beam size was determined from the beam profile (Fig. 6). The sizes and intensities are listed in Table 1 for beams from both the 5 µm and 10 µm pinholes. The data for the focused full beam (no mini-beam collimator, upstream slits open) and for the beam defined by closing the upstream slits to their minimum aperture were reported previously (Sanishvili *et al.*, 2008). Measurements with the upstream slits set to 20 µm × 20 µm are included in the table for comparison.

The mini-beams had a more desirable round shape relative to the elliptical 'standard' focused beam. Nevertheless the mini-beams from both the 5 µm and 10 µm pinholes were slightly smaller in the vertical direction than in the horizontal even though the mini-beams are considerably smaller than the full beam in the vertical direction. The ellipticity of the mini-beams (horizontal:vertical ratio) was twofold to fourfold smaller than for the full beam (Table 1). The intensity stability of the mini-beam is typically 1–2% RMS over time periods from 0.1 s to 30 min (sampled on a 1 ms interval), and <3% RMS over 12 h.

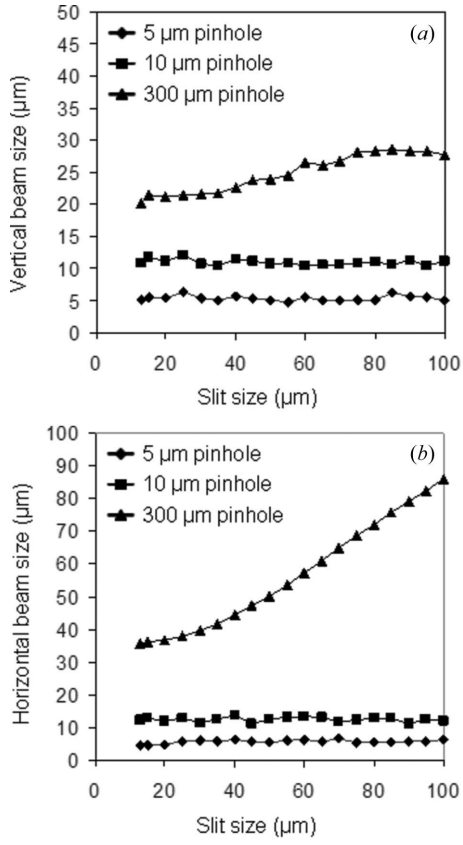

Figure 5
Effect of slit setting on beam size at the sample position in the (*a*) vertical and (*b*) horizontal directions. The slits were 230 mm upstream of the sample position. The beam size was recorded at the sample position using a knife-edge scan as described in the text. The minimum setting of the slits was 13 µm, but beams of this size were not achievable at the sample position when the slits defined the beam. In contrast, the mini-beam size is almost constant over a wide range of upstream slit settings for beams defined by the 5 µm and 10 µm mini-beam collimators.

The angular dispersion of the beam was measured at the sample position by placing a Si(220) analyzer crystal (15.8 µrad intrinsic rocking-curve width) on the goniometer and recording the diffracted beam intensity as a function of goniometer angle. These measurements were made with the beam focused at the sample position. The same ion chamber that was used for the beam intensity measurements was positioned to record the diffracted intensity from the analyzer crystal. The results for the full beam and for the beam defined by the 10 µm pinhole are shown in Fig. 7. The full beam had an angular dispersion of 136.6 µrad that was reduced to 103.3 µrad by the 10 µm pinhole. (The rocking-curve width of the analyzer crystal contributes about 1 µrad to the measured values assuming the widths add in quadrature.) Because the

goniometer axis of rotation was oriented in the horizontal plane, the angular dispersion could be measured only in the vertical direction. However, the mini-beam should reduce the horizontal dispersion more than the vertical given the greater decrease in horizontal beam size.

3.4. Back-scatter guard

One of the main benefits of using a mini-beam with small sample crystals is to minimize background on diffraction images owing to secondary scatter from air and the sample mount. Indeed we discovered that the intense focused X-ray beam impinging on the Pt pinhole, even though it was imbedded 2.4 mm inside the bullet-shaped scatter guard, generated backward scatter sufficiently intense to produce a high background on the CCD detector (MARMosaic 300 detector, Rayonix LLC, formerly Mar USA, Inc.) used to record diffraction data from sample crystals. The back-scatter guard was essential to remove this source of background. The back-scatter guard and forward-scatter tube were so successful in reducing background that the 300 µm aperture in the triple collimator is used in routine operations because of its benefits for background reduction, even though this aperture does not define the beam.

Table 1
Measured beam size and intensity for the 5 µm and 10 µm pinholes, the full beam size reduced using the slits and the focused full beam on 23-ID-B.

Nominal beam defining aperture	Beam size, FWHM (V × H) (µm)	Beam size ratio (horizontal/vertical)	Intensity [photons s^{-1} $(100\ mA)^{-1}$]†
23-ID-B with beam focused at the sample position			
5 µm‡	4.8 × 6.2	1.3	4.7×10^{10}
10 µm‡	10.6 × 11.6	1.1	2.2×10^{11}
20 µm × 20 µm slits	17.4 × 36.7	2.1	5.8×10^{11}
50 µm × 100 µm slits	23.6 × 87.2	3.7	3.6×10^{12}
Full beam	28 × 135	4.8	5.5×10^{12}
Fully optimized beam focused at the sample position			
Full beam (23-ID-B)	25 × 120	4.8	1.0×10^{13}
Full beam (23-ID-D)	20 × 65	3.3	2.0×10^{13}

† The intensity measurements were made at energies of 12.00 keV for 23-ID-B and 12.66 keV for 23-ID-D. ‡ Measurements were taken with the upstream slits set to 50 µm × 100 µm. Similar beam sizes were measured with the 5 µm and 10 µm pinholes on 23-ID-D. The beam intensity through these pinholes on 23-ID-D is two to four times greater than on 23-ID-B owing to differences in the insertion device and in the size of the focused full beam.

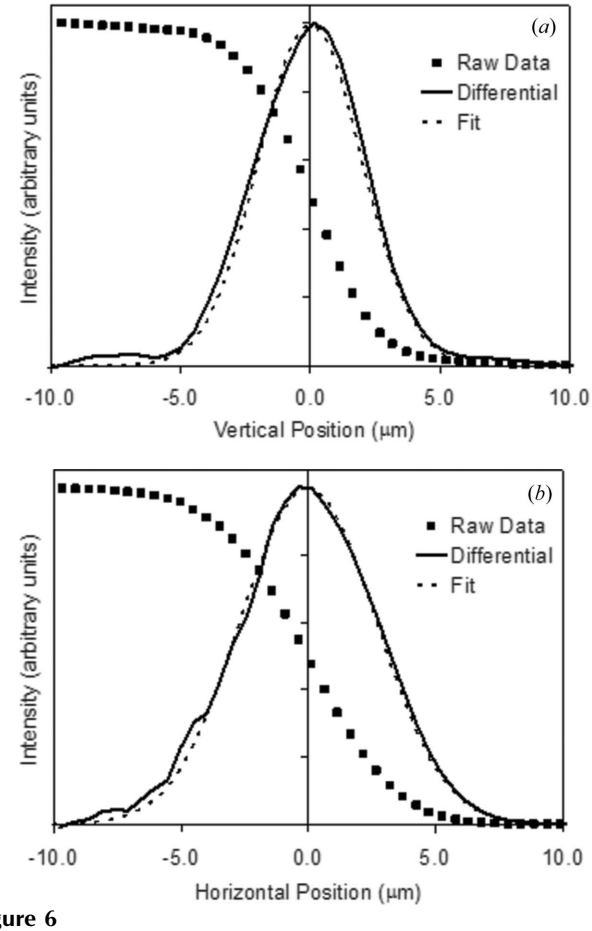

Figure 6
Profiles of the mini-beam defined by the 5 µm aperture in the vertical (*a*) and horizontal (*b*) directions. Profiles were recorded at the sample position using a knife-edge scan as described in the text. The raw knife-edge scans were differentiated, providing the beam profile (solid line). An error function was fit to the raw data (not shown). The best-fit Gaussian is derived from the derivative of the error function (dashed line).

3.5. Background reduction

To quantitate the reduction in background owing to the mini-beam, scattering patterns were recorded without a sample (air scatter) and with samples of several typical crystallization solutions frozen in loops. For each of the samples, 10 s exposures were recorded with the CCD detector using an unattenuated X-ray beam (E = 12.0 keV) with the upstream beam-defining slits set to 50 µm × 100 µm for the 5 µm and 10 µm mini-beams and the 300 µm scatter guard on 23-ID-B.

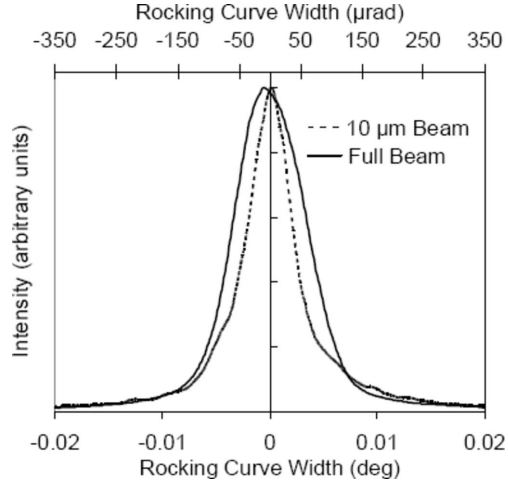

Figure 7
Vertical angular dispersion of the mini-beam. Rocking curves of a Si(220) analyzer crystal located at the sample position were recorded for the full beam (solid line) and for the mini-beam defined by the 10 µm aperture (dashed line).

The CCD detector was 250 mm from the sample position. The intensity in individual pixels was averaged azimuthally resulting in an experimental curve of integrated intensity *versus* reciprocal coordinate [$q = 2\sin(\theta)/\lambda$]. For each sample the scattered intensity curves were directly proportional to the incident beam intensity for all q-values recorded, indicating that the mini-beam collimator (5 µm or 10 µm pinhole) captured scatter from the pinhole as effectively as the scatter guard (300 µm pinhole) captured scatter from the upstream beam-defining slits.

Each of the crystallization solutions scattered more strongly than air, supporting the argument that background can be reduced by maximizing the ratio of sample-crystal volume to solution volume illuminated by the beam. Background measurements from a protein crystal are consistent with the sample-free background measurements. Background reduction in diffraction images recorded on 23-ID-D from a typical protein crystal [frozen in 30%(*w*/*v*) PEG 400, 10%(*v*/*v*) glycerol, 500 m*M* NaCl, 120 m*M* buffer] was 25-fold for the 10 µm mini-beam relative to a 21 µm × 35 µm beam (defined with the upstream slits set to 50 µm × 50 µm and the 300 µm scatter guard).

The benefit of background reduction when the beam size is reduced to be smaller than the crystal has been demonstrated (Fig. 4 of Sanishvili *et al.*, 2008). The diffracted intensity in any given reflection is lower with the mini-beam than with the full beam because both the intensity and illuminated crystal volume are lower. However, the background is reduced by a larger factor, leading to an improved signal-to-noise ratio.

3.6. Implementation in the user program

The triple collimator has been in routine use on the GM/CA-CAT undulator beamlines since February 2008. At the start of each user run the beamline staff align the full beam to the cross-hairs of the on-axis camera. Then the positions of the 5 µm and 10 µm collimators are checked and aligned to the cross-hairs if necessary, and the new positions are stored. This allows rapid switching among 5 µm, 10 µm and standard (300 µm) apertures without re-alignment. The triple collimator is controlled through the *Blu-Ice* user interface (McPhillips *et al.*, 2002; Stepanov *et al.*, 2004, 2006). According to the requirements of individual samples, users can switch rapidly between standard and mini-beams by a simple pull-down menu in *Blu-Ice*. Owing to its robustness and convenience, the triple collimator has been received with great enthusiasm by users, who are rapidly learning the benefits of a mini-beam for routine data collection.

4. Discussion and conclusion

The high intensity and low divergence available in the focused undulator beam of third-generation synchrotron sources combined with the design of the mini-beam apparatus provide a simple means to define a 5–10 µm beam with high intensity and low divergence. The beam shape is almost circular, resulting in small round diffraction maxima (reflections) whose sizes are often limited by the point-spread function of the CCD detector, typically ∼100 µm, and by the crystal mosacity. This improves the signal-to-noise ratio relative to the 'standard' full beam by reduction of the number of pixels contributing background to each reflection. The initial prototype of the mini-beam collimator did not incorporate a back-scatter guard. Although the pinhole was a few millimeters inside the bullet-shaped scatter guard, the X-ray background reaching the CCD detector was high. The intense focused beam impinging on the pinhole generated back-scatter, which was re-scattered from air and/or from the camera lens. The background scattering was reduced by the addition of the back-scatter guard (Figs. 1 and 2) and by positioning the mini-beam collimator so that the gap between the back-scatter guard and the lens was reduced to about 0.5 mm (Fig. 3). (The concave surface of the compound objective lens limits how close the collimator can approach the lens and still be moved up out of the beam.) In this configuration, background scattering (in the absence of a sample) reaching the CCD detector was reduced to ∼3 counts pixel^{-1} s^{-1} for the 5 µm beam, compared with ∼790 counts pixel^{-1} s^{-1} for the full beam (recorded 250 mm downstream of the sample position on a CCD detector with 100 µm point-spread function and 73.2 µm pixels at $q = 25.1$ nm^{-1}, $d = 2.5$ Å). This further improves the signal-to-noise ratio by reduction of the per-pixel background in diffraction images.

The pinhole horizontal/vertical position defines the position of the beam at the sample location. The two high-precision motorized stages provide a very stable highly reproducible position of the pinhole and hence the mini-beam. The alignment of the mini-beam to the rotation axis of the goniometer is stable over periods of 12–24 h. This feature is invaluable in user operations because users can reliably and frequently switch between standard and mini-beams according to the properties of individual samples.

The focused beam is an image of the source and hence is sensitive to beam motions. At the APS, transverse motions of the particle beam are typically of the order of 1 µm RMS. These motions and the image of the source are demagnified by the focusing mirrors and hence do not contribute to mini-beam intensity fluctuations. However, angular variations in the trajectory of the particle beam through the undulator can be a serious problem. For example, the angular resolution of the APS particle-beam trajectory, based on positional feedback from the radio-frequency beam-position monitors (RF-BPMs), is less than 0.1 µrad in the frequency range 0.016–30 Hz (Decker & Singh, 2005). Thus, at the positions of the focusing mirrors, typically with a 3 mrad angle of incidence, the X-ray beam can move 4.8 µm on 23-ID-B and 6.4 µm on 23-ID-D, resulting in the X-ray beam moving a few millimeters along the mirror surface. Even with modern bimorph mirrors, beam movement coupled with the small residual slope error can defocus or redirect portions of the beam, thereby moving the beam relative to the pinhole and causing intensity fluctuations. This source of positional instability has been greatly reduced by photon BPMs, which were added recently to the APS feedback system (Singh & Decker, 2001). The BPMs are

located at 18.5 m from the center of the straight section for 23-ID-B and at 20.5 m for 23-ID-D. These BPMs minimize long-term drift of the X-ray beam and provide sub-μrad stability to the feedback system owing to their long distance from the source.

In addition to source variations, even small imperfections in beamline X-ray optics can amplify source motion, resulting in beam motion of the order of several micrometers at the sample position. An advantage of the biomorph mirrors is that the slope error can be minimized *in situ*. Thus sub-μrad slope errors can be achieved, resulting in a beam of uniform profile both at the focus and far from the focus. The lack of structure in the focused beam minimizes intensity fluctuations if the beam moves along the mirror surface. Many sources of instability were anticipated and eliminated in the design of the 23-ID beamline optics; many others were discovered and mitigated during commissioning. Attention to many such details, as well as the approach of overfilling a small aperture near the sample, resulted in a mini-beam that is stable in position even if the focused beam moves slightly.

In combination, the high degree of positional reproducibility and stability of the mini-beam apparatus, the positional stability of the focused X-ray beam, and the approach of overfilling the aperture provide a mini-beam with high-intensity stability [0.5% over short (ms) and long (30 min) time scales]. The beam intensity measured with the intensity-feedback system running is stable to 1–2% over long (12 h) time scales. Thus the mini-beam has the requisite stability for measurement of one diffraction image as well as an entire data set. The intensity-feedback system improves long-term stability of the mini-beam, but increases short-term (2–5 s) intensity noise and is a user-selectable option. It should be noted that simply building or purchasing a microdiffractometer does not ensure a stable mini-beam. The beamline must deliver a stable beam to the end-station instruments.

The pinhole selects the central part of the focused beam. Thus the mini-beam and the focused full beam have approximately the same flux density. Their main difference is a smaller diameter and lower total flux for the mini-beam. For most samples the mini-beam illuminates fewer unit cells than the standard beam does, resulting in significantly lower counts in diffraction maxima. However, because the mini-beam apparatus provides such low background, the signal-to-noise ratio is improved with the mini-beam relative to the focused full beam for sample crystals that do not fully intercept the full beam. With equal flux densities, the mini-beam and full beam should have similar rates of radiation damage (Sliz *et al.*, 2003). However, the effects of radiation damage can be mitigated by rastering the mini-beam across a large crystal and collecting partial data sets from several spots, thereby reducing radiation damage to each spot on the crystal (Rasmussen *et al.*, 2007). The improved signal-to-noise with the mini-beam allows one to use a large crystal more efficiently. This is especially important for multi-wavelength anomalous diffraction experiments in which two to six times more data are recorded than for monochromatic non-resonance experiments. Mitigating radiation sensitivity or poor crystal quality can extend the *de facto* diffraction limit of many crystals.

The focused full beam has low divergence (∼137 μrad, 0.008°) and is therefore well suited to fully resolving reflections from crystals with unit cells of 1000 Å or larger (Gan & Johnson, 2008). The mini-beam has even lower divergence (∼103 μrad, 0.006°, Fig. 7) and thus is suitable for data collection from crystals with large unit cells (Laurberg *et al.*, 2008). Approaches to achieving a small beam by only focusing generally also increase beam divergence. For example, the mono-bounce capillary focusing optic used at MacCHESS focuses to a 20 μm beam at the sample, but is limited by the 2000 μrad (0.11°) divergence downstream of the sample. The short focusing mirrors on ID23-2 of the ESRF are configured with a high demagnification ratio of 20–25:1, providing a focused beam of less than 10 μm at the sample position. However, the beam divergence is about 250–300 μrad (0.014–0.017°).

An important design goal of the mini-beam apparatus was to visualize the sample during data collection with the on-axis high-resolution camera. The cross section of the mini-beam collimator was designed to be as small as possible to minimize the fraction of the lens that was obscured. The taper of the bullet-shape scatter guard on the single collimator matches the subtended angle of the scatter tube at the sample location. Optical studies showed that the mini-beam single and triple collimators degrade the image of the crystal only slightly. Nevertheless, the best image for optical alignment of the sample crystal is obtained by moving the mini-beam collimator up out of the center of the optical path with the high-precision stages.

The success of the mini-beam in the GM/CA-CAT user program relied on successful integration of the mini-beam collimators into the *Blu-Ice* beamline control software, which was developed at SSRL (McPhillips *et al.*, 2002) and adapted to the EPICS environment with several modifications at GM/CA-CAT (Stepanov *et al.*, 2004, 2006). Pre-set positions for individual collimators are stored in an EPICS database, allowing quick exchange of collimators. The new triple collimator allows the pre-set positions to be recalled by users without manual exchange and rarely needs tweaking.

The mini-beam has several advantages for macromolecular crystallography (Sanishvili *et al.*, 2008). By tailoring the beam size to the crystal size, the ratio of irradiated crystal volume (diffracting) to irradiated mount volume (background scattering) can be controlled. Thus for small crystals a significant improvement in the signal-to-noise ratio is observed with the mini-beam owing to the dramatic reduction in background scattering from the non-diffracting volume supporting the crystal (for example, Cherezov *et al.*, 2007).

The mini-beam can also be beneficial for large but imperfect crystals. In cases of high mosaicity, split or smeared diffraction peaks or multiple lattices the mini-beam may be used to selectively irradiate a more homogeneous or ordered region of the crystal, allowing measurement of data of higher quality than would be possible with the full beam.

The mini-beam is also a useful probe to find the best regions for data collection from large crystals. Once the best region has been located, the standard beam may be used for data collection. This approach is greatly facilitated by the triple collimator.

Problems of crystal size, radiation sensitivity, high mosaicity and crystal inhomogeneity are extremely common. In this respect the most important aspect of the mini-beam apparatus described here is arguably its full integration into the user controls of the two GM/CA-CAT 23-ID beamlines. Switching among the full beam and the 5 μm and 10 μm mini-beams is simple, rapid and robust. In the first running period with the mini-beam triple collimator, three-quarters of GM/CA-CAT user groups applied the mini-beam to their problematic samples.

GM/CA CAT is supported by Federal funds from the National Cancer Institute (Y1-CO-1020) and the National Institute of General Medical Science (Y1-GM-1104). Use of the Advanced Photon Source was supported by the US Department of Energy, Basic Energy Sciences, Office of Science, under contract No. DE-AC02-06CH11357. We thank B. K. Kobilka and W. I. Weis of Stanford University for helpful discussions and suggestions during initial mini-beam experiments; F. Cipriani of EMBL-Grenoble for helpful discussions; G. Decker, L. Emery and K. Schroeder of APS for improvements to the APS beam stabilization and helpful discussions.

References

Cherezov, V., Rosenbaum, D. M., Hanson, M. A., Rasmussen, S. G., Thian, F. S., Kobilka, T. S., Choi, H. J., Kuhn, P., Weis, W. I., Kobilka, B. K. & Stevens, R. C. (2007). *Science*, **318**, 1258–1265.

Cipriani, F., Felisaz, F., Lavault, B., Brockhauser, S., Ravelli, R., Launer, L., Leonard, G. & Renier, M. (2007). *Ninth International Conference on Synchrotron Radiation Instrumentation*, edited by J.-Y. Choi and S. Rah, pp. 1928–1931. New York: American Institute of Physics.

Coulibaly, F., Chiu, E., Ikeda, K., Gutmann, S., Haebel, P. W., Schulze-Briese, C., Mori, H. & Metcalf, P. (2007). *Nature (London)*, **446**, 97–101.

Decker, G. & Singh, O. (2005). *Proceedings of the 2005 Particle Accelerator Conference*, Knoxville, TN, USA, pp. 3268–3270 (http://www.jacow.Org/p05/papers/rpae053.pdf).

Fischetti, R. F., Yoder, D. W., Xu, S., Stepanov, S., Makarov, O., Benn, R., Corcoran, S., Diete, W., Schwörer-Böhing, M., Signorato, R., Schröder, L., Berman, L., Viccaro, P. J. & Smith, J. L. (2007). *Ninth International Conference on Synchrotron Radiation Instrumentation*, edited by J.-Y. Choi and S. Rah, pp. 754–757. New York: American Institute of Physics.

Fotinou, C., Emsley, P., Black, I., Ando, H., Ishida, H., Kiso, M., Sinha, K. A., Fairweather, N. F. & Isaacs, N. W. (2001). *J. Biol. Chem.* **276**, 32274–32281.

Gan, L. & Johnson, J. E. (2008). *J. Synchrotron Rad.* **15**, 223–226.

Huang, R. & Bilderback, D. H. (2006). *J. Synchrotron Rad.* **13**, 74–84.

Laurberg, M., Asahara, H., Korostelev, A., Zhu, J., Trakhanov, S. & Noller, H. F. (2008). *Nature (London)*, **454**, 852–857.

McPhillips, T. M., McPhillips, S. E., Chiu, H.-J., Cohen, A. E., Deacon, A. M., Ellis, P. J., Garman, E., Gonzalez, A., Sauter, N. K., Phizackerley, R. P., Soltis, S. M. & Kuhn, P. (2002). *J. Synchrotron Rad.* **9**, 401–406.

Moukhametzianov, R., Burghammer, M., Edwards, P. C., Petitdemange, S., Popov, D., Fransen, M., McMullan, G., Schertler, G. F. X. & Riekel, C. (2008). *Acta Cryst.* D**64**, 158–166.

Nelson, R., Sawaya, M. R., Balbirnie, M., Madsen, A., Riekel, C., Grothe, R. & Eisenberg, D. (2005). *Nature (London)*, **435**, 773–778.

Pebay-Peyroula, E., Rummel, G., Rosenbusch, J. P. & Landau, E. M. (1997). *Science*, **277**, 1676–1681.

Perrakis, A., Cipriani, F., Castagna, J.-C., Claustre, L., Burghammer, M., Riekel, C. & Cusack, S. (1999). *Acta Cryst.* D**55**, 1765–1770.

Rasmussen, S. G., Choi, H. J., Rosenbaum, D. M., Kobilka, T. S., Thian, F. S., Edwards, P. C., Burghammer, M., Ratnala, V. R., Sanishvili, R., Fischetti, R. F., Schertler, G. F., Weis, W. I. & Kobilka, B. K. (2007). *Nature (London)*, **450**, 383–387.

Renault, L., Hanzal-Bayer, M. & Hillig, R. C. (2001). *Acta Cryst.* D**57**, 1167–1170.

Riekel, C. (2004). *J. Synchrotron Rad.* **11**, 4–6.

Riekel, C., Burghammer, M. & Schertler, G. (2005). *Curr. Opin. Struct. Biol.* **15**, 556–562.

Sanishvili, R., Nagarajan, V., Yoder, D., Becker, M., Xu, S., Corcoran, S., Akey, D. L., Smith, J. L. & Fischetti, R. F. (2008). *Acta Cryst.* D**64**, 425–435.

Signorato, R., Hignette, O. & Goulon, J. (1998). *J. Synchrotron Rad.* **5**, 797–800.

Singh, O. & Decker, G. (2001). *Proceedings of the 2001 Particle Accelerator Conference*, Chicago, IL, USA, pp. 539–543 (http://accelconf.web.cern.ch/accelconf/p01/papers/roab008.pdf).

Sliz, P., Harrison, S. C. & Rosenbaum, G. (2003). *Structure*, **11**, 13–19.

Stepanov, S., Makarov, O., Urakhchin, A., Devarapalli, S., Yoder, D. W. & Fischetti, R. F. (2006). *NOBUGS-2006 Conference Program and Abstracts*, LBL, Berkeley, CA, USA, pp. 31–32 (http://www.bnl.gov/bnlweb/pubaf/abstract.asp?recid = 3169).

Stepanov, S., Makarov, O., Urakhchin, A., Schwabe, U., Venkataraman, C. & Pugliese, R. (2004). *NOBUGS-2004 Conference Program and Abstracts*, Paul Scherrer Institute, Villigen PSI, Switzerland (http://lns00.psi.ch/nobugs2004/papers/paper00118.pdf).

Weichendrieder, O., Wild, K., Strub, K. & Cusack, S. (2000). *Nature (London)*, **408**, 167–173.

Xiao, B., Spencer, J., Clements, A., Ali-Khan, N., Mittnacht, S., Broceño, C., Burghammer, M., Perrakis, A., Marmorstein, R. & Gamblin, S. J. (2003). *Proc. Natl. Acad. Sci.* **100**, 2363–2368.

Xu, S. & Fischetti, R. F. (2007). *Proc. SPIE*, **6665**, 1–8.

Xu, S., Fischetti, R. F., Benn, R. & Corcoran, S. (2007). *Ninth International Conference on Synchrotron Radiation Instrumentation*, edited by J.-Y. Choi and S. Rah, pp. 1403–1406. New York: American Institute of Physics.

Zhou, M., Morais-Cabral, J. H., Mann, S. & MacKinnon, R. (2001). *Nature (London)*, **411**, 657–661.